Electron cloud observations and cures in the Relativistic Heavy Ion Collider

W. Fischer,* M. Blaskiewicz, J. M. Brennan, H. Huang, H.-C. Hseuh, V. Ptitsyn, T. Roser, P. Thieberger, D. Trbojevic,
J. Wei, and S. Y. Zhang

Brookhaven National Laboratory, Upton, New York 11973, USA

U. Iriso

CELLS, 08193 Bellaterra, Spain

Since 2001, the Relativistic Heavy Ion Collider has experienced electron cloud effects, some of which have limited the beam intensity. These include dynamic pressure rises (including pressure instabilities), tune shifts, a reduction of the instability threshold for bunches crossing the transition energy, and possibly incoherent emittance growth. We summarize the main observations in operation and dedicated experiments as well as countermeasures including baking, nonevaporable getter coated warm beam pipes, solenoids, bunch patterns, antigrazing rings, prepumped cold beam pipes, scrubbing, and operation with long bunches.

PACS numbers: 29.20.db, 29.27.Bd

I. INTRODUCTION

The Relativistic Heavy Ion Collider (RHIC), in operation since 2000, has collided species from gold ions at energies up to 100 GeV/nucleon, to polarized protons at energies up to 100 GeV [1,2]. The two independent superconducting rings are named "Blue" and "Yellow". Since 2001, dynamic pressure rises were observed that limited the beam intensity. At that time the cause of the dynamic pressure rise was not known and electron clouds were suspected as a possible mechanism. With ever increasing beam intensities other phenomena were seen that were also caused by electron clouds.

Here we summarize these observations as well as the countermeasures tested and used. Table I shows selected machine and beam parameters relevant to electron clouds for all species RHIC has operated with so far.

Most electron cloud observations are indirect. Such indirect observations include the effect of electron clouds on the vacuum pressure, coherent tune shifts, beam instabilities, and emittance growth. Direct observations were made with electron detectors, and correlated with pressure observation.

After electron clouds were established as the likely leading cause for dynamic pressure rises, a number of cures were tested or implemented. *In situ* baking, installation of beam pipes coated with a nonevaporable getter (NEG) material, prepumping of the cold regions, and scrubbing aim at improving the surface conditions. The use of solenoids and antigrazing rings reduces the number of electrons and molecules released from the surface. Optimized bunch patterns and the operation with longer bunches reduce the electron cloud buildup.

II. OBSERVATIONS

Observations of effects caused by electron clouds were made during machine operation and in dedicated experiments. The most common observation is a dynamic pressure rise caused by electron-impact desorption after an electron cloud has been formed. Other observations include coherent tune shifts, direct electron observations with electron detectors, beam instabilities and beam loss, and possibly incoherent emittance growth. Although an early calculation [3] raised the possibility of an increased heat load due to electron clouds with 110 bunches, no increased heat load has been observed so far.

A. Dynamic pressure rise

Large dynamic pressure rises were observed in 2001 (Fig. 1) when the first attempt was made to double the number of bunches from 55 to 110. At that time the origin of the beam induced pressure rise was not known. A number of possible sources were considered initially,

TABLE I. Main machine and beam parameters relevant to electron clouds for all species RHIC has operated with [2].

| Parameter	Unit	Au	Cu	d	p
Atomic number Z	$\cdots$	79	29	1	1
Mass number A	$\cdots$	197	63	2	1
Revolution time τ	μs	12.8	12.8	12.8	12.8
Rigidity, injection	Tm	81	81	81	79
Rigidity, store	Tm	832	832	832	334
Full bunch length, injection	ns	15	15	15	20
Full bunch length, store	ns	5	5	5	10
Bunch spacing t_b	$\cdots$	Multiples of 108 ns			
Number of bunches N_a	$\cdots$	Up to 111			
Ions per bunch N_b	10^9	1.0	50	110	200

*Wolfram.Fischer@bnl.gov
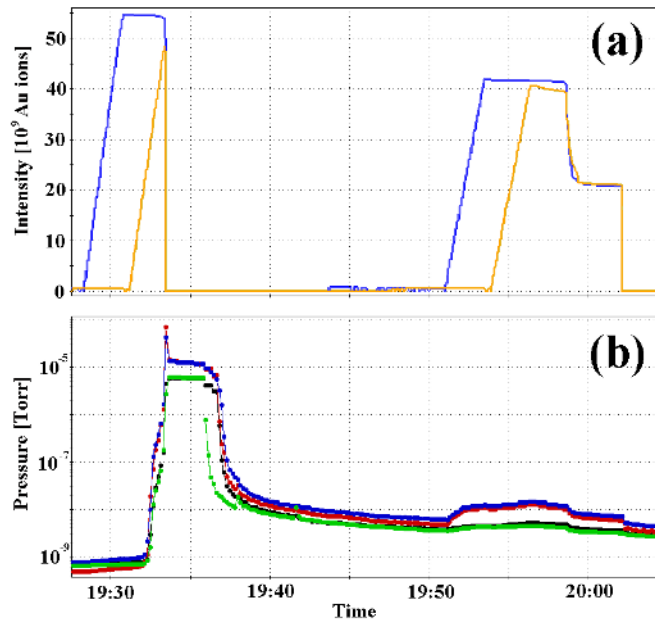
FIG. 1. (Color) The first two attempts to fill both rings with 110 bunches, twice the design number (October 2001) [14]. Intensities of the two RHIC rings, named Blue and Yellow are shown in part (a) and the pressure measured at four gauges in an interaction region is shown in part (b).

namely ion-impact desorption after residual gas ionization and subsequent acceleration of the ions in the beam potential, ion-impact desorption after beam loss, and electron-impact desorption after an electron cloud has been formed.

Dynamic pressure rise from electron-impact desorption is also observed in other machines [4–7]. Ion-impact desorption after residual gas ionization led to pressure instabilities in the ISR [8]. Ion-impact desorption is typically a problem in lower energy machines with charge-exchange processes where beam losses cannot be easily localized, like the AGS Booster [9,10], SIS18 [10–12], or LEIR [13]. Desorption after beam loss occurs when halo particles hit the beam pipe under grazing incidence. At the time of the first dynamic pressure rise in RHIC ion-impact desorption coefficients for ions in the GeV/nucleon energy range were not known.

Dynamic pressure rise was the first and still is the most common electron cloud observation in RHIC [14–16]. The dynamic pressure rise has been observed with all species (p, d, Cu, Au) at injection, transition (protons do not cross the transition energy), and store (Figs. 1, 3, and 4).

We consider a vacuum model that includes a static gas load Q_0, a load Q_1 of desorbed gas molecules induced by electrons in a cloud hitting the walls, a load Q_2 from residual gas molecules ionized by the cloud electrons and accelerated by the beam, a load Q_3 from residual gas molecules ionized and accelerated by the beam, and a load Q_4 from desorption after lost beam ions hit the chamber wall. The total load is then

$$Q = Q_0 + Q_1 + Q_2 + Q_3 + Q_4. \quad (1)$$

A gas load Q is given by

$$Q = kT\frac{dN_{\text{gas}}}{dt}, \quad (2)$$

where k is the Boltzmann constant, T the absolute temperature, and dN_{gas}/dt the number of molecules released per unit time. In equilibrium

$$Q = SP, \quad (3)$$

where S is the pumping speed and P the pressure. For the warm regions we consider periodic vacuum sections with pumps of speed $2S$, separated by the distance $2L$. The load Q_1 from a beam pipe section of length L is

$$Q_1 = kT\frac{L}{e}\frac{dI_e}{dl}\eta_e, \quad (4)$$

where e is the elementary charge, dI_e/dl the electron current into the wall per unit length, and η_e the average desorption coefficient for the energy distribution of the cloud electrons. The load Q_2 from a beam pipe section of length L can be estimated as [compare with Eq. (6) below]

$$Q_2 = \sigma_e P \frac{2rL}{e}\frac{dI_e}{dl}\eta_{\text{ion}}, \quad (5)$$

where σ_e is the cross section for residual gas ionization for cloud electrons, r the beam pipe radius, and η_{ion} the average desorption coefficient for ions accelerated by the beam. Values for σ_e can be found in Ref. [17]. The gas load Q_3 is [18]

$$Q_3 = \sigma_b PL\dot{N}_{\text{tot}}\eta_{\text{ion}}, \quad (6)$$

where σ_b is the cross section for the residual gas ionization, $\dot{N}_{\text{tot}}$ is the beam particle flow, i.e., the number of particles in the beam divided by the revolution time. Values for σ_b can be found in Refs. [18,19]. The load Q_4 from the length L is

$$Q_4 = kTL\frac{d^2N_{\text{tot}}}{dldt}\eta_{\text{ionloss}}, \quad (7)$$

where $d^2N_{\text{tot}}/dldt$ is the beam intensity loss rate per unit length, and η_{ionloss} the average desorption coefficient for lost beam ions. η_{ionloss} is different from η_{ion} because the lost beam ions have a much higher energy than the ions generated by residual gas ionization and accelerated by the beam, and because they are lost under grazing incidence while the ions generated by residual gas ionization are lost under close to perpendicular impact.

In equilibrium we have $PS = Q$, where S is the pumping speed. Introducing the parameter

$$b = \sigma_e\frac{2r}{e}\frac{dI_e}{dl} + \sigma_b\dot{N}_{\text{tot}}, \quad (8)$$

we obtain an expression for the equilibrium pressure measured at the pump

$$P = \frac{Q_0 + kTL(\frac{1}{e}\frac{dI_e}{dl}\eta_e + \frac{d^2N_{tot}}{dldt}\eta_{ionloss})}{S - \eta_{ion}Lb}. \quad (9)$$

We will now compare the gas loads created by the various processes (Table III to Table VI). For all processes we will give estimates for the warm vacuum system for Au and p beams, assuming H_2 or CO as the dominant gas, and for unbaked and baked surfaces. Without a dynamic pressure increase, H_2 is the dominant gas in the warm vacuum regions. With dynamic pressure increase, the fraction of heavier molecules, like CO, increases.

For an estimate of the gas load Q_1 [Eq. (1)] due to electron-impact desorption from an electron cloud, shown in Table III, we need the electron current into the wall, and the ion-impact desorption coefficients. For an unbaked surface we use $dI_e/dl = 20$ mA/m, a value obtained from simulations in Ref. [20], and electron-impact desorption coefficients from *in situ* measurements with electron detectors (see Refs. [21,22] and below). For both H_2 and CO this gives a gas load 3 orders of magnitude larger than the static load (see Fig. 2). For baked surfaces we reduce

the electron current into the wall by an order of magnitude, and again use a desorption coefficient from Refs. [21,22] (see below), also obtained through *in situ* measurements.

For an estimate of the gas load Q_2 [Eq. (5)] due to residual gas ionization by cloud electrons, subsequent acceleration of the ions in the electromagnetic field of the beam, and ion-impact desorption, we assume that the pressure is already elevated to 10^{-7} Torr (Table IV). The average electron energy is again taken from a simulation in Ref. [20], and the ionization cross sections from Ref. [17]. The average ion energy at the wall is calculated with [27]

$$E_{ion} = \frac{e^2ZN_b}{2\pi\epsilon_0 s_b}\ln\left(\frac{r}{\sigma_r}\right), \quad (10)$$

where Z is the ion charge state and N_b are the number of particles per bunch, s_b the bunch spacing, and σ_r the rms beam radius. Ion-impact desorption coefficients for ions in the energy range of tens of eV (Table IV) are not well documented. We use Ref. [18], where numbers can be obtained by interpolating between zero and an energy higher than the energy of interest. We assume that the error
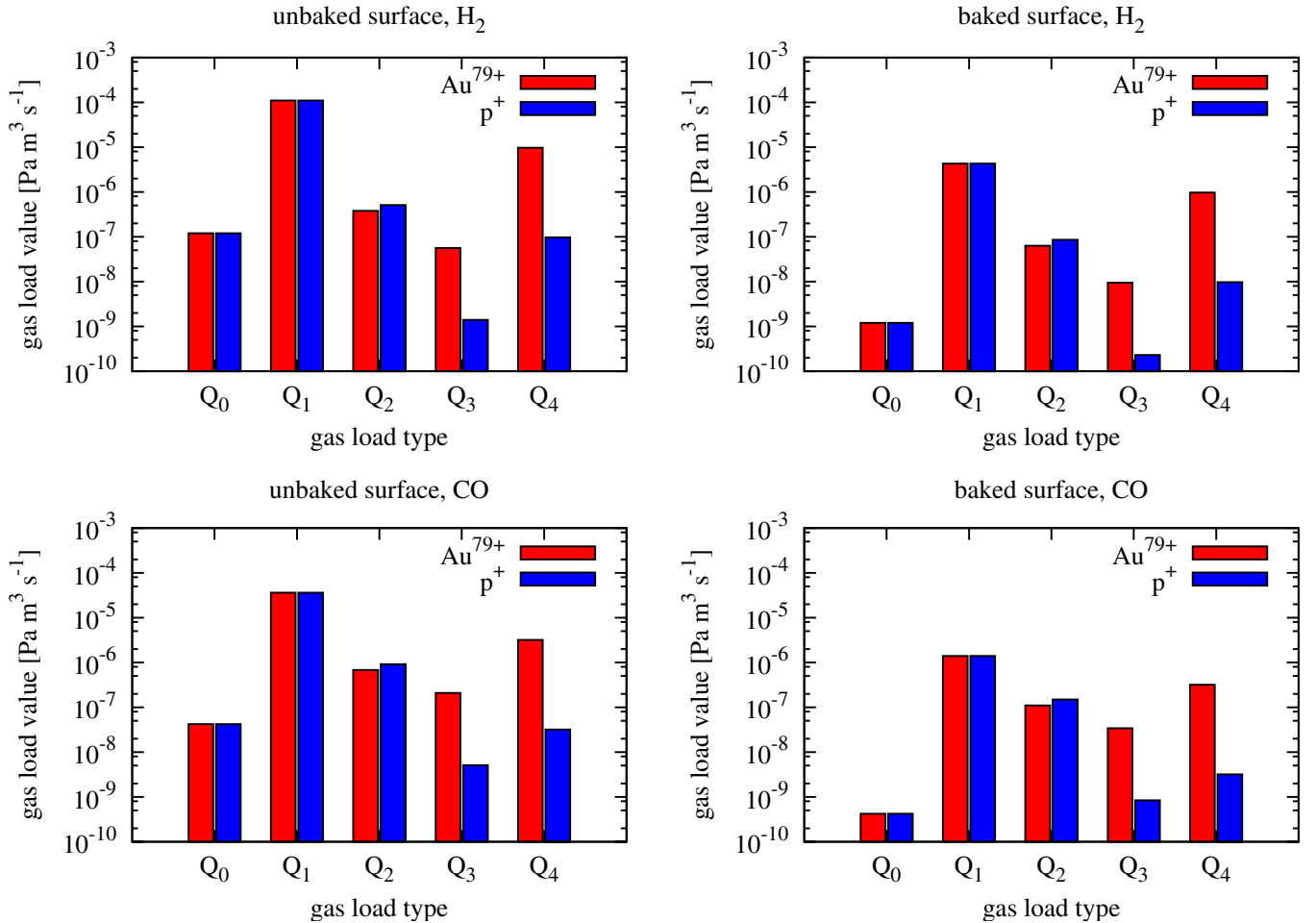

FIG. 2. (Color) Comparison of gas loads due to various effects. This figure is a summary of the gas load calculations presented in Tables II, III, IV, V, and VI.

on the ion-impact desorption coefficients used is at least a factor of 2. Figure 2 shows that, with these assumptions, the gas load Q_2 is about 2 orders of magnitude lower than the gas load Q_1.

In order to calculate the load Q_3 [Eq. (6)], we need the ionization cross section $\sigma_{b,j}$ for a beam particle of charge Ze hitting a molecule j. This can be written as [28,29]

$$\sigma_j = 1.874 \times 10^{-24} \text{ m}^2 \frac{Z^2}{\beta^2}(M_j^2 x + C_j), \qquad (11)$$

where M_j^2 and C_j are coefficients specific to the molecule and $x = 2\ln(\beta\gamma) - \beta^2$ is a function of the relativistic beam parameters β and γ. Using the same dynamic pressure, average ion energy at the wall, and ion-impact desorption coefficients as in Table IV, the estimated gas loads Q_3 are shown in Table V. Figure 2 shows that the loads Q_3 are lower than the loads Q_2.

An estimate of the gas load Q_4 [Eq. (7)] from desorption due to lost beam ions has a large error. The beam lifetime can vary over a wide range and the beam loss varies widely over the circumference. In order not to underestimate the effect, we assume here that beam is lost at a rate of $1\%/\text{s}$ of the total intensity (corresponding to only 1.7 min beam lifetime) into the length L (Table VI). Such a low beam lifetime is not typical for operation. We take estimates for the desorption coefficients from Refs. [23–26]. These too have large errors, up to an order of magnitude. In our estimate we assume that desorption coefficients for baked surfaces are an order of magnitude lower than for unbaked surfaces, in line with earlier measurements [18]. With these assumptions the load Q_4 is lower than the load Q_1 by an order of magnitude for Au ions, and by 2–3 orders of magnitude for protons (Fig. 2).

Figure 2 summarizes our gas load estimates and shows that the gas load Q_1 dominates, i.e., electron-impact desorption from electrons in a cloud is the leading cause of dynamic pressure rise. We will further strengthen this conclusion below, when electron detector and pressure data are presented together, showing a linear relationship between average electron cloud density and pressure increase.

Before closing this section we mention two more vacuum phenomena: the pressure rise at transition [30,31], and the pressure rise in one of the experiments [32,33]. At transition the bunches are shortest, and the beams typically lose a few percent of their intensity when crossing the transition energy. The pressure rise occurs before beam loss is visible, and when sorted into bunch patterns (Fig. 3) the pressure rise is approximately proportional to the bunch intensity above a certain threshold. This feature is consistent with electron cloud simulations [30]. Transition pressure rises have also been observed at the Fermilab Main Ring [7].

The PHOBOS experiment (now decommissioned) had a 12 m long uncoated beryllium beam pipe. After rebucket-
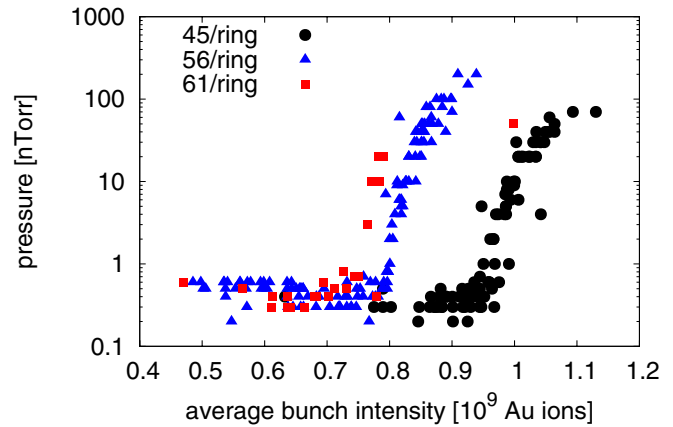

FIG. 3. (Color) Transition pressure rise in IR12 with Au beams as a function of the average bunch intensity. The bunch intensity is averaged over the Blue and Yellow ring intensities, and the values before and after transition. The data are further separated into ramps with 45, 56, and 61 bunches per ring. The dots show the maximum pressure at or shortly after transition [30].

ing, when the bunches are transferred from an $h = 360$ to an $h = 2520$ harmonic system and their length is shortened to half, an increase in the pressure by approximately 1 order of magnitude was observed (Fig. 4, Ref. [33]). The high pressure led to increased and often unacceptable experimental background. It was observed to switch off suddenly after a time interval ranging from 30 min to 2 h. The sudden switch-off cannot be explained by simple electron-impact desorption. In simulations, the electron cloud density shows no second order phase transitions when the bunch intensity is changed by a small amount. Such a phase transition can be explained with the assumption of both an electron and ion cloud [32].
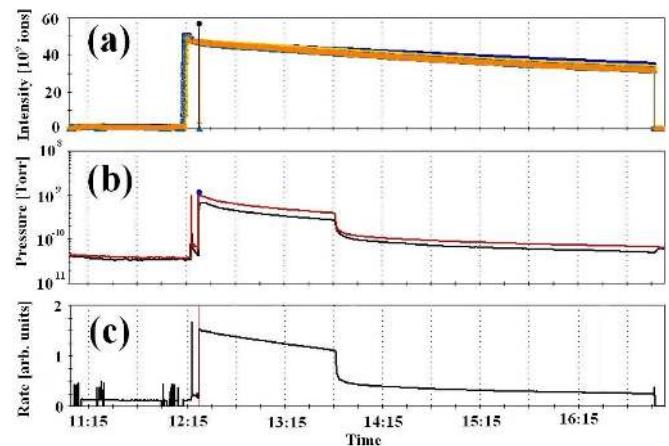

FIG. 4. (Color) Pressure rise in the PHOBOS experimental area after rebucketing with 56 bunches. The beam intensities in the Blue and Yellow ring (a) slowly decay during a store, and the pressure measured in 2 gauges (b) drops sharply after some time. With high pressure the experimental background (c) is increased [33].
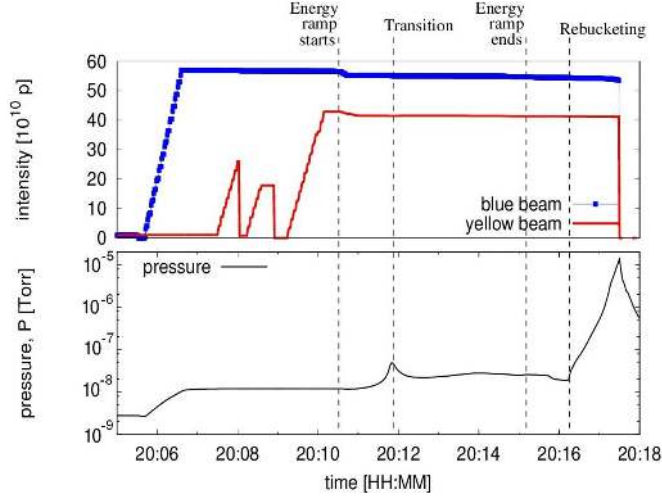
FIG. 5. (Color) A pressure instability with Au beam in the Blue ring. The upper part shows the total intensity for both rings during injection, acceleration, and storage. The lower part shows the pressure in the Blue collimator region, with an exponential increase after rebucketing [35].

B. Pressure instabilities

In some instances, pressure instabilities could be observed where the pressure grows exponentially without bounds until the beam is aborted by the beam permit system [34,35]. This only occurred with gold beam, in unbaked locations, and after an electron cloud was formed after the bunches were shortened by a factor 2. Figure 5 shows the pressure in an unbaked collimator region, which also has a geometry and materials different from most of the other warm regions. The formation of an electron cloud can be triggered after the bunch length is reduced, when bunches are transferred from the accelerating rf system into the storage rf system. From Eq. (9) a stability condition can be derived. However, in conductance limited systems a more stringent condition applies and the maximum desorption coefficient $\eta_{\text{crit,ion}}$ becomes [18]

$$\eta_{\text{crit,ion}} = \frac{\pi^2}{4} \frac{c}{bL^2}. \tag{12}$$

From the observed growth times τ_P, ranging from 6 to 12 s, one can also calculate the ion-impact desorption coefficient as [35,36]

$$\eta_{\text{ion}} = |\omega_0 c + \pi r^2/\tau_P|/b, \tag{13}$$

where ω_0 is the smallest root of the equation

$$(\omega L)\tan(\omega L) = SL/c. \tag{14}$$

Table VII shows estimates for the critical desorption coefficients, and desorption coefficients calculated from the observed pressure growth times. The parameters in the table are slightly different from the parameters in Tables II, III, IV, V, and VI to reflect our best estimates of the conditions in the warm collimator region at the time.

The estimated critical ion-impact desorption coefficient $\eta_{\text{crit,ion,CO}}$ for Au beams and CO molecules is close to the ion-impact desorption coefficient $\eta_{\text{ion,CO}}$ estimated from the pressure growth time τ_P, showing the possibility of a pressure instability for this beam and gas molecule. This is not the case for H_2 molecules and no pressure instabilities were observed with protons, even with the highest intensities available at injection. The estimated ion-impact desorption coefficients $\eta_{\text{ion,H2}}$ and $\eta_{\text{ion,CO}}$ are an order of magnitude larger than those from Ref. [18] that we used to estimate the gas loads Q_2 and Q_3. If the ion-impact desorption coefficients η_{ion} were generally larger, the gas loads Q_2 and Q_3 would also be larger than the estimates shown in Tables IV and V. But even if the η_{ion} values were larger by an order of magnitude, this would not change the conclusion that the gas load Q_1 from electron-impact desorption dominates.

C. Tune shift

After dynamic pressure rises were observed, the coherent tune shift along a bunch train was measured at injection (Fig. 6, Ref. [20]). The sign of the observed tune shift in both planes is consistent with the existence of electron clouds, and the value of the tune shift allowed a first estimate of the electron cloud density.

In a round chamber, a proton bunch passing each turn through a static electron cloud with uniform spatial density ρ_e experiences a coherent tune shift [37–39]

$$\Delta Q_{x,y} = \rho_e \left(\frac{r_p Z}{\gamma A} \right) \frac{\beta_{x,y} L_{\text{ec}}}{2}, \tag{15}$$

where $\beta_{x,y}$ are the average beta functions for the horizontal and vertical plane, respectively, L_{ec} the length of the

TABLE II. Main parameters of the warm vacuum system.

parameter	Unit	Value
Beam pipe radius r	m	0.06
Temperature T	K	300
Tube conductance c_{H2}	$m^4\,s^{-1}$	0.75
Tube conductance c_{CO}	$m^4\,s^{-1}$	0.25
Pumping speed $2S_{H2}$	$m^3\,s^{-1}$	0.94
Pumping speed $2S_{CO}$	$m^3\,s^{-1}$	0.31
Distance between pumps $2L$	m	14
Unbaked surface		
Static pressure P_0	Torr	1.0×10^{-9}
Static pressure P_0	Pa	1.3×10^{-7}
Static gas load for H_2, $Q_{1,H2}$	$Pa\,m^3\,s^{-1}$	1.2×10^{-7}
Static gas load for CO, $Q_{1,CO}$	$Pa\,m^3\,s^{-1}$	4.8×10^{-8}
Baked surface		
Static pressure P_0	Torr	1.0×10^{-11}
Static pressure P_0	Pa	1.3×10^{-9}
Static gas load for H_2, $Q_{1,H2}$	$Pa\,m^3\,s^{-1}$	1.2×10^{-9}
Static gas load for CO, $Q_{1,CO}$	$Pa\,m^3\,s^{-1}$	4.8×10^{-10}

TABLE III. Estimate of gas load Q_1 in the warm vacuum regions due to electron-impact desorption from electron clouds.

Parameter	Unit	Au^{79+}	p	Comment
Unbaked surface				
Electron current into wall dI_e/dl	Am^{-1}	0.02	0.02	From simulation in Ref. [20]
Electron-impact desorption coefficient for H_2, $\eta_{e,H2}$	$\cdots$	0.03	0.03	See Ref. [21,22] and text
Electron-impact desorption coefficient for CO, $\eta_{e,CO}$	$\cdots$	0.01	0.01	See Ref. [21,22] and text
Gas load for H_2 from length L, $Q_{1,H2}$	$Pa\,m^3\,s^{-1}$	1.1×10^{-4}	1.1×10^{-4}	
Gas load for CO from length L, $Q_{1,CO}$	$Pa\,m^3\,s^{-1}$	3.6×10^{-5}	3.6×10^{-5}	
Baked surface				
Electron current into wall dI_e/dl	Am^{-1}	0.002	0.002	Reduced by factor 10 from unbaked
Electron-impact desorption coefficient for H_2, $\eta_{e,H2}$	$\cdots$	0.002	0.002	See Ref. [21,22] and text
Electron-impact desorption coefficient for CO, $\eta_{e,CO}$	$\cdots$	0.004	0.004	See Ref. [21,22] and text
Gas load for H_2 from length L, $Q_{1,H2}$	$Pa\,m^3\,s^{-1}$	4.3×10^{-6}	4.3×10^{-6}	
Gas load for CO from length L, $Q_{1,CO}$	$Pa\,m^3\,s^{-1}$	1.4×10^{-6}	1.4×10^{-6}	

TABLE IV. Estimate of gas load Q_2 in the warm vacuum regions due to residual gas ionization by cloud electrons, subsequent acceleration of the ions by the beam, and ion-impact desorption.

Parameter	Unit	Au^{79+}	p	Comment
Dynamic pressure P	Torr	1.0×10^{-7}	1.0×10^{-7}	
Dynamic pressure P	Pa	1.3×10^{-5}	1.3×10^{-5}	
Average electron energy E_e	eV	50	50	From simulation in Ref. [20]
Ionization cross section for H_2, $\sigma_{e,H2}$	m^2	9.8×10^{-21}	9.8×10^{-21}	See Ref. [17]
Ionization cross section for CO, $\sigma_{e,CO}$	m^2	2.2×10^{-20}	2.2×10^{-20}	See Ref. [17]
Average ion energy at wall E_{ion}	eV	23	31	Equation (10), see Ref. [27]
Unbaked surface				
Ion-impact desorption coefficient for H_2, $\eta_{ion,H2}$	$\cdots$	0.6	0.8	See Ref. [18]
Ion-impact desorption coefficient for H_2, $\eta_{ion,CO}$	$\cdots$	0.4	0.6	See Ref. [18]
Gas load for H_2 from length L, $Q_{2,H2}$	$Pa\,m^3\,s^{-1}$	3.8×10^{-7}	5.1×10^{-7}	
Gas load for CO from length L, $Q_{2,CO}$	$Pa\,m^3\,s^{-1}$	6.8×10^{-7}	9.2×10^{-7}	
Baked surface				
Ion-impact desorption coefficient for H_2, $\eta_{ion,H2}$	$\cdots$	0.09	0.13	See Ref. [18]
Ion-impact desorption coefficient for H_2, $\eta_{ion,CO}$	$\cdots$	0.07	0.10	See Ref. [18]
Gas load for H_2 from length L, $Q_{2,H2}$	$Pa\,m^3\,s^{-1}$	6.3×10^{-8}	8.6×10^{-8}	
Gas load for CO from length L, $Q_{2,CO}$	$Pa\,m^3\,s^{-1}$	1.1×10^{-7}	1.5×10^{-7}	

TABLE V. Estimate of gas load Q_3 in the warm vacuum regions due to residual gas ionization by the beam, subsequent acceleration of the ions by the beam, and ion-impact desorption. The dynamic pressure, ion-energy at the wall, and ion-impact desorption coefficients assumed here are the same as in Table IV.

Parameter	Unit	Au^{79+}	p	Comment
Ionization cross section for H_2, $\sigma_{b,H2}$	m^2	1.3×10^{-19}	2.2×10^{-23}	See Ref. [29]
Ionization cross section for CO, $\sigma_{b,CO}$	m^2	5.8×10^{-19}	1.0×10^{-22}	See Ref. [29]
Unbaked surface				
Gas load for H_2 from length L, $Q_{3,H2}$	$Pa\,m^3\,s^{-1}$	5.6×10^{-8}	1.4×10^{-9}	
Gas load for CO from length L, $Q_{3,CO}$	$Pa\,m^3\,s^{-1}$	2.1×10^{-7}	5.1×10^{-9}	
Baked surface				
Gas load for H_2 from length L, $Q_{3,H2}$	$Pa\,m^3\,s^{-1}$	9.4×10^{-9}	2.3×10^{-10}	
Gas load for CO from length L, $Q_{3,CO}$	$Pa\,m^3\,s^{-1}$	3.4×10^{-8}	8.4×10^{-10}	

TABLE VI.   Estimate of gas load Q_4 in the warm vacuum regions due to beam loss.

Parameter	Unit	Au^{79+}	p	Comment
Relative beam loss rate in length L	$\% s^{-1}$	1.0	1.0	
Absolute beam loss rate in length L	s^{-1}	1.1×10^9	1.1×10^{11}	
Unbaked surface				
Ion-impact desorption coefficient for H$_2$, $\eta_{ionloss,H2}$	$\cdots$	3×10^5	30	See Refs. [23–26]
Ion-impact desorption coefficient for H$_2$, $\eta_{ionloss,CO}$	$\cdots$	1×10^5	10	See Refs. [23–26]
Gas load for H$_2$ from length L, $Q_{4,H2}$	$Pa\, m^3\, s^{-1}$	9.7×10^{-6}	9.7×10^{-8}	
Gas load for CO from length L, $Q_{4,CO}$	$Pa\, m^3\, s^{-1}$	3.2×10^{-6}	3.2×10^{-8}	
Baked surface				
Ion-impact desorption coefficient for H$_2$, $\eta_{ionloss,H2}$	$\cdots$	3×10^4	3	See Refs. [23–26]
Ion-impact desorption coefficient for H$_2$, $\eta_{ionloss,CO}$	$\cdots$	1×10^4	1	See Refs. [23–26]
Gas load for H$_2$ from length L, $Q_{4,H2}$	$Pa\, m^3\, s^{-1}$	9.7×10^{-7}	9.7×10^{-9}	
Gas load for CO from length L, $Q_{4,CO}$	$Pa\, m^3\, s^{-1}$	3.2×10^{-7}	3.2×10^{-9}	

TABLE VII.   Estimates for the critical ion-impact desorption coefficients $\eta_{crit,ion}$ for Au ions at store, and p at injection with the highest injected intensities during the RHIC run in 2004. Pressure instabilities were observed with Au, but not with p.

Parameter	Unit	Au^{79+}	p
Number of bunches N_a	$\cdots$	56	111
Particles per bunch N_b	10^9	1.0	170
Vacuum system			
Pressure P_0	Torr	1.0×10^{-8}	
Temperature T	K	300	
Pipe radius r	m	0.08	
Conductance c_{H2}	$m^4\, s^{-1}$	0.56	
Conductance c_{CO}	$m^4\, s^{-1}$	0.15	
Space between pumps $2L$	m	11.4	
Ionization by cloud electrons			
Current into wall dI_e/dl	A/m	0.03	
Average electron energy	eV	50	
Cross section $\sigma_{e,H2}$	m^2	9.8×10^{-21}	
Cross section $\sigma_{e,CO}$	m^2	2.2×10^{-20}	
Ionization by beam			
Cross section $\sigma_{b,H2}$	m^2	1.3×10^{-19}	2.2×10^{-23}
Cross section $\sigma_{b,CO}$	m^2	5.8×10^{-19}	1.0×10^{-22}
Ion-impact desorption			
Ion energy at wall	eV	15	62
Parameter b_{H2} [Eq. (8)]	$m^2\, s^{-1}$	1.0×10^{-3}	3.3×10^{-4}
Parameter b_{CO} [Eq. (8)]	$m^2\, s^{-1}$	4.0×10^{-3}	8.1×10^{-4}
Desorption coefficient $\eta_{crit,ion,H2}$	$\cdots$	42	131
Desorption coefficient $\eta_{crit,ion,CO}$	$\cdots$	2.8	14
Reported $\eta_{ion,H2}$ [18]	$\cdots$	0.4	1.5
Reported $\eta_{ion,CO}$ [18]	$\cdots$	0.3	1.2
Pressure instability			
Measured P growth time τ_P	s	6–12	N/A
Corresponding $\eta_{ion,H2}$	s	23–21	N/A
Corresponding $\eta_{ion,CO}$	s	2.1–1.7	N/A

sections with electron clouds, and $r_p = 1.5347 \times 10^{-18}$ m the classical proton radius. With this simple model, electron cloud densities of order $\rho_e = 10^{11}$–10^{12} m^{-3} were estimated. The lower estimate is for the assumption of electron clouds in the whole ring, the higher estimate for the assumption of electron clouds in the warm regions only.

The estimated electron cloud densities also made possible the first comparisons with simulations [20]. For the simulations the code CSEC [40] was employed which was originally developed by one of the authors (M. B.) for the PSR and SNS [41]. CSEC uses the model of Ref. [42] for the secondary electron generation. Electron cloud densities of the same order of magnitude could be obtained in the simulations. The simulation results are sensitive to a number of input parameters which are not very well known [20]. The coherent tune shift due to electron clouds has not created any operational problems.
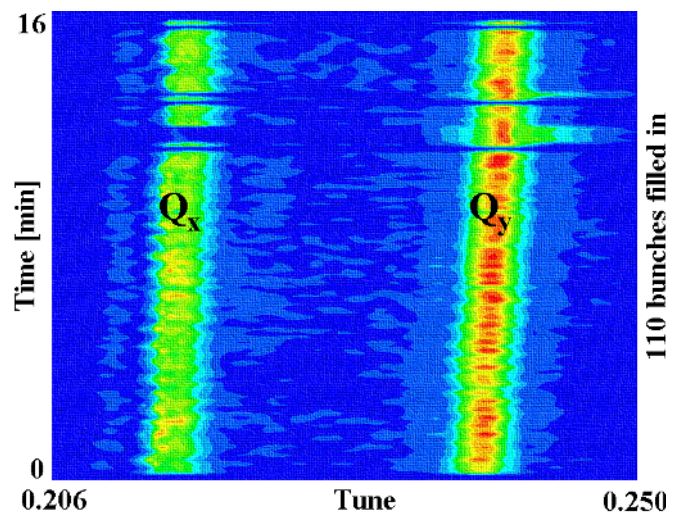

FIG. 6.   (Color) Coherent tunes of the last injected bunch along a train of 110 proton bunches with 108 ns spacing in the Yellow ring. Because of coupling both transverse tunes are visible [20].
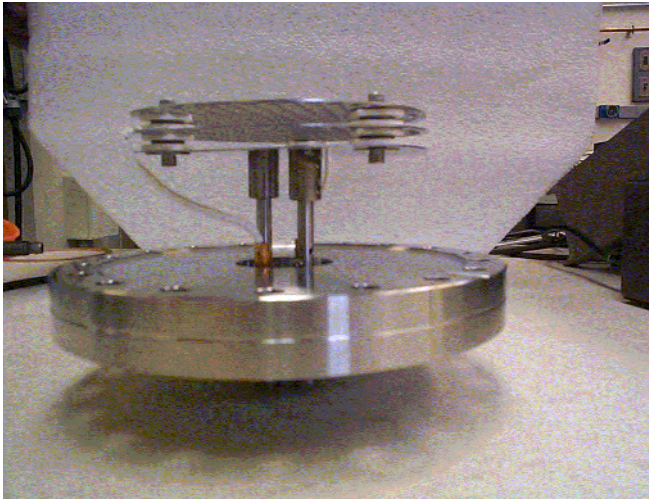
FIG. 7. (Color) Multigrid electron detector in RHIC. The grids have a diameter of 12 cm [43].

D. Electrons

Shortly after the first electron cloud observations were made, 15 electron detectors were installed in the warm regions [43,44]. The detector design is based on a PSR design [45], and similar detectors have been installed in other machines, like APS [46], SPS [47], and BEPC [48].

With the multigrid design (Fig. 7) it is possible to sample the cloud density, and determine the energy distribution of the electrons in the cloud. In Fig. 8 such a measurement is shown for a train of 43 proton bunches, 108 ns apart, with an average bunch intensity of 1.6×10^{11}. Forty-three bunches fill about one-third of the RHIC circumference. Over the length of the bunch train the electron cloud
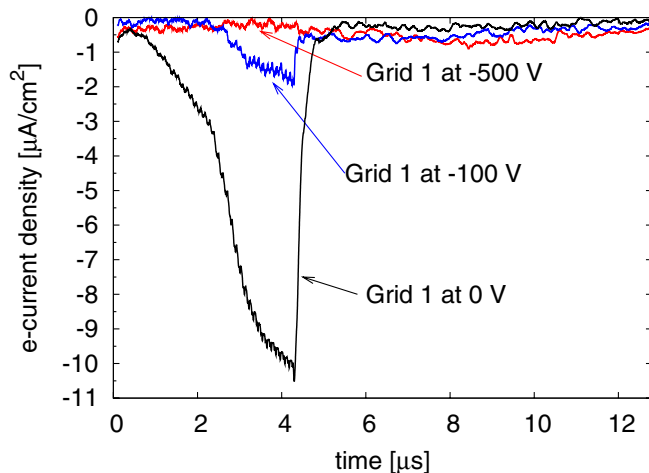
buildup is visible. With the variable voltage on grid 1, electrons below a certain energy can be rejected, and this allows a measurement of the electron energy spectrum.

Relevant factors for the electron-impact desorption are the electron cloud density averaged over one turn τ, the electron energy spectrum, and the electron-impact desorption coefficient η_e. The time-averaged electron cloud density is proportional to the time-averaged voltage of the electron cloud detector

$$\langle V \rangle_\tau = \frac{1}{\tau} \int_0^\tau V(t) dt, \tag{16}$$

where $V(t)$ is the instantaneous voltage signal of the electron detector. The RHIC electron detectors are ac coupled to the system electronics. To calculate a nonzero average over one turn, we shift the baseline by the maximum value in the electron detector snapshot. The average over one revolution is then calculated by

$$\frac{1}{\tau} = \int_0^\tau V(t) dt = \frac{1}{N_s} \sum_{i=1}^{N_s} [V_i - V_{\max}], \tag{17}$$

where N_s is the number of samples in one revolution. With a calibration [21,22] this voltage can be translated into a an electron current density dI/dA into the wall. Figure 9 shows this time-averaged electron current density together with a pressure reading from a vacuum gauge nearby, as Blue beam is injected. Using the same data as in Fig. 9, Fig. 10 depicts the pressure increase as a function of the average electron current density into the wall, which can be well fitted to a linear function. The linear fit shows that the dynamic pressure rise is dominated by electron-impact desorption.

FIG. 8. (Color) Measured instantaneous electron current density into the wall of a train of 43 proton bunches, 108 ns apart, with an average bunch intensity of 1.6×10^{11}. With increasing voltage on grid 1, electrons below certain energies are rejected, allowing the measurement of electron energy spectrum in the cloud [43].
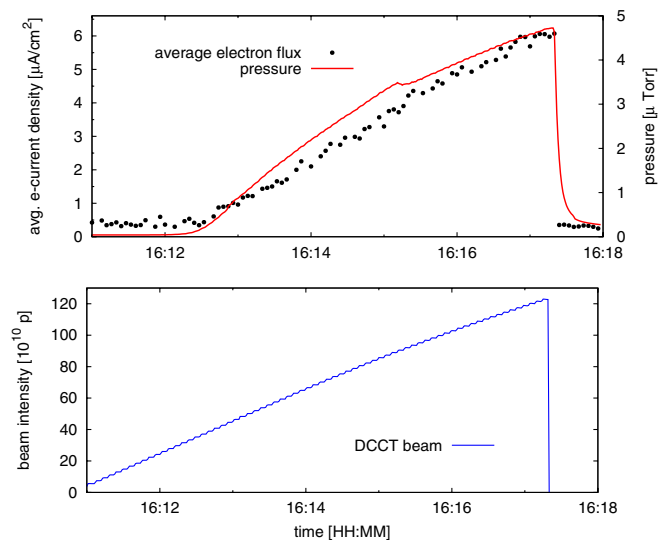

FIG. 9. (Color) Measured pressure and time-averaged electron current density into the wall (top), as Blue beam is being injected (bottom) [21,22].
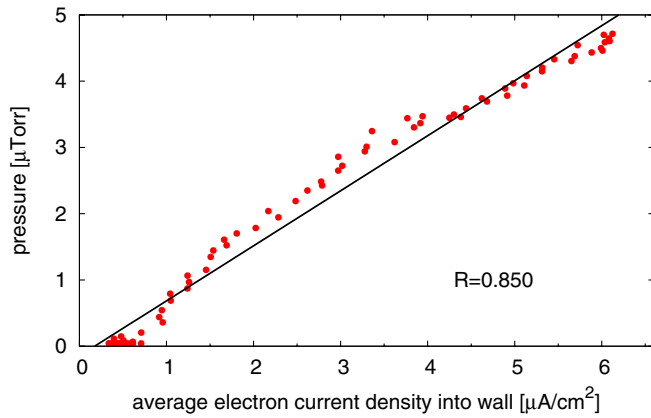
FIG. 10. (Color) Pressure increase vs time-averaged electron current density into the wall. Red dots are measured values, the black line is a linear fit [21,22].

Figure 11 exhibits two measured energy spectra. These show a major contribution from low energy electrons below 10 eV, and extends to energies of about 300 eV. Data below 5 eV cannot be taken due to experimental limitations. The measured energy spectrum can be reproduced in simulations, also shown in Fig. 11 [21,22].

Electron-impact desorption coefficients η_e can also be extracted from measured electron cloud densities and pressure increases using Eq. (5). This is shown in Fig. 12. For an unbaked stainless steel beam pipe $\eta_e = 0.01 \pm 0.005$ molecules/electron (CO equivalent) is measured, after several months of conditioning in operation. The initial value is larger by approximately a factor 5. For a baked stainless steel pipe no conditioning is observable, and the measured electron-impact desorption coefficient is $\eta_e = 0.004 \pm 0.001$ [21,22].
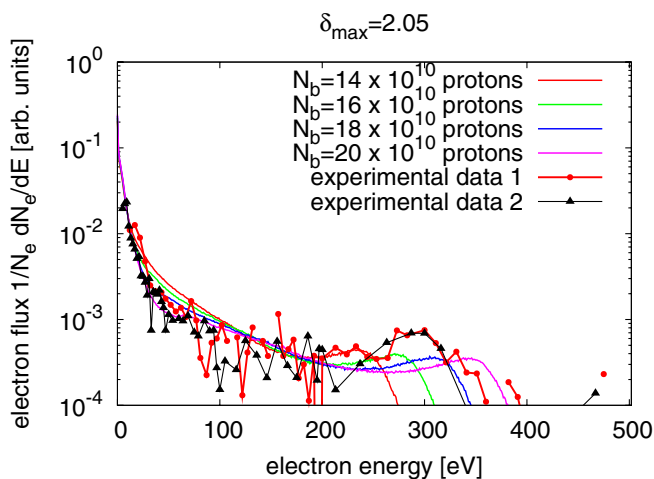
FIG. 11. (Color) Energy spectrum measured, and simulated for $\delta_{\max} = 2.05$ and different bunch intensities. The spectrum shape is not significantly affected by the $\delta_{\max}$, but depends on the beam parameters (bunch intensity, length, etc.) [21,22].
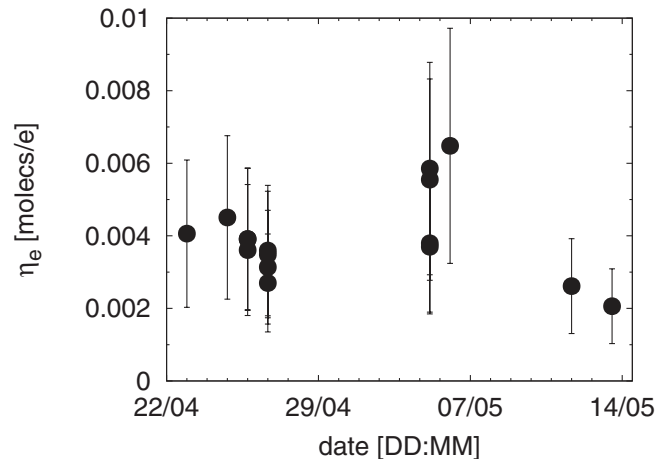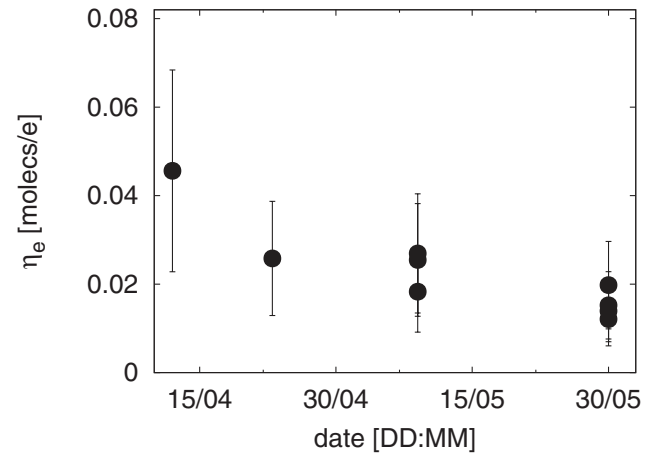
FIG. 12. Calculated desorption coefficients for the unbaked stainless steel surface BO2 (top), and the baked stainless steel surface at IR12. The error bar (50%) stems from the systematic uncertainty in the pumping speed and vacuum pressure readings. A decrease of the desorption coefficient with time is noticeable for the unbaked stainless steel (top) due to the scrubbing effect [21,22].

E. Beam instabilities

In RHIC the beam is most susceptible to instabilities during transition crossing. All species except protons cross the transition energy. Because the main magnets are superconducting, their ramp rate is slow, and transition crossing is facilitated with a γ_t-jump of fast ramping quadrupoles. Because the bunches are short and the chromaticity across the transition energy is changed much more slowly than the γ_t-jump, bunches with enough intensity can become unstable. The observed instabilities are single bunch and transverse [49]. Two typical growth times were observed, 15 ms and 120 ms. In addition to carefully chosen chromaticity settings, octupoles are used near transition to suppress instabilities. It was found that electron clouds, also enhanced by the short bunch length at transition, can reduce the intensity instability threshold. This manifests itself through increasing beam losses along the bunch train, and was observed in dedicated experiments with varying

W. FISCHER *et al.*

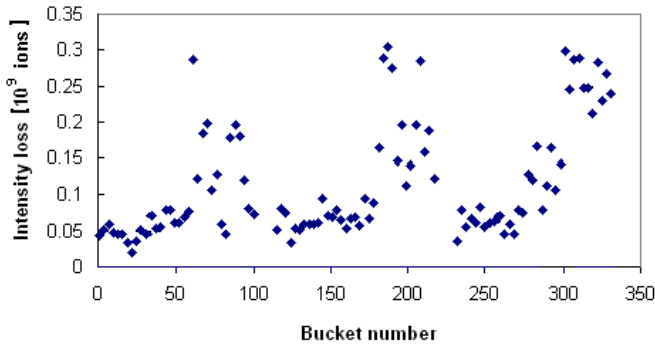Phys. Rev. ST Accel. Beams **11,** 041002 (2008)

FIG. 13. (Color) Yellow beam loss at transition as a function of position in the bunch train. In this pattern 8 bunches are missing after 1/3 and 2/3 of the bunch train length. The bunch train is followed by the abort gap. The intensity losses per bunch increase until a gap is reached, and then fall back because the electron cloud decays.

octupole and gap voltage settings [50], as well as during operation. Figure 13 [51] shows an example from the recent Au run. A review of single bunch instabilities driven by electron clouds is given in Ref. [52].

F. Emittance growth

Incoherent emittance growth from electron clouds was investigated in Refs. [53–56], and may also be relevant to the RHIC polarized proton operation. In the 2006 polarized proton run, bunches shortened through rf quadrupole pumping in the AGS were injected in order to increase the luminosity through the reduction of the hourglass effect at store. However, the luminosity of the stores with bunches of reduced length was lower than the luminosity of stores with longer bunches of comparable intensity (Fig. 14) [57,58]. At the same time, a higher dynamic pressure was observed at injection. This could be an indication that electron clouds at injection have increased the proton beam emittance. But with only a few stores with short-bunch injection, causes for emittance growth other than electron clouds cannot yet be ruled out. In a separate test the emittance growth of bunches with 2×10^{11} protons at injection was measured to be 40 mm mrad/h [16].

III. CURES

After the first observation of electron cloud effects, a number of cures were tested and some were implemented
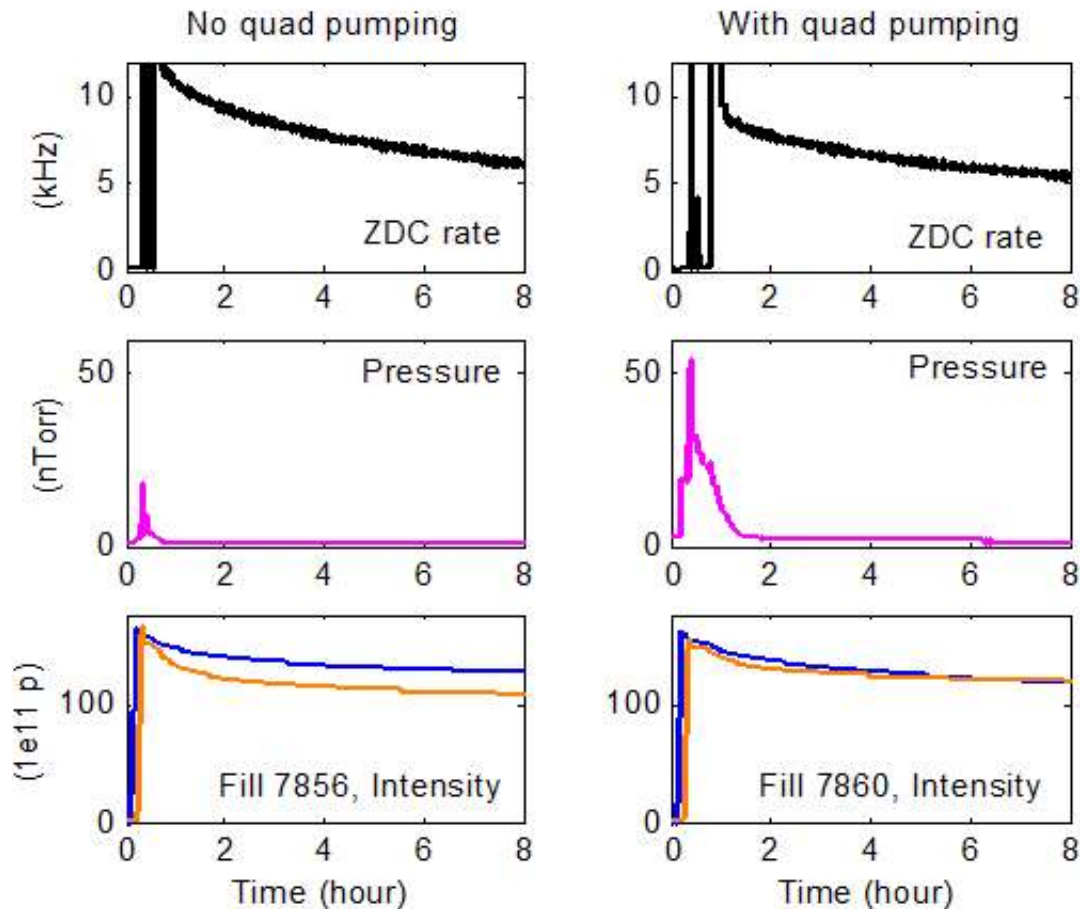

FIG. 14. (Color) Event rates from collisions, sum of pressure in 4 warm locations, and beam intensity for two stores. The left column shows the standard situation, the right column shows a store for which shorter bunches were injected from the AGS [57].

on a larger scale. Cures tested or implemented include *in situ* baking, NEG coated warm beam pipes, solenoids, optimized bunch patterns, antigrazing rings, prepumping of cold beam sections, scrubbing, and operation with longer bunches.

A. *In situ* baking

The RHIC beam pipes in the warm regions are made of stainless steel 304L (beam pipes of the cold regions are made of 316LN). At the manufacturer the drawn tubes were detergent cleaned, water rinsed, acid prickled with $HF + HNO_3$, water rinsed again, annealed at 1050°C for 10 min, and then quenched. At BNL the pipes were cut to length, and the end flanges welded. Pipes for installation in magnets were baked under vacuum at 350°C for 24 h before delivering to the magnet manufacturer.

Because of scheduling constraints, most warm beam pipes were not baked *in situ* initially. After the first dynamic pressure rises were observed, a program was started to bake *in situ* all warm pipes. This is possible at all locations, with the exception of the warm rf, and a few places where instruments are located. The program yielded the first significant increase in the beam intensity.

B. NEG coating

Thin-film coating of beam pipes with the nonevaporable getter material TiZrV has been developed at CERN [59,60], and found large-scale application in a number of machines including ESRF [61], RHIC [62,63], LEIR [13], SOLEIL [64], and LHC [65].

The properties of typically 1 μm thick NEG coatings were measured, including activation dependent secondary electron yield (SEY), pumping speed, induced desorption, and performance deterioration due to venting cycles. After 2 h of activation at 200°C, NEG coated surfaces can reach a SEY of 1.1, and have pumping speeds of approximately $0.5 \, 1 \, s^{-1} \, cm^{-2}$ for H_2, and initially $5 \, 1 \, s^{-1} \, cm^{-2}$ for CO [65–68]. However, the pumping speed deteriorates with repeated venting and activation. After 10 venting/heating cycles, the pumping speed is reduced by about an order of magnitude [65].

In RHIC, 55 m of NEG coated beam pipes were installed in 2003, for tests in 2004, and for comparisons with beam pipe sections that had been wrapped with solenoids. After evaluation, a decision was made to replace as much of the approximately 700 m of warm beam pipe as possible with NEG coated one. This is possible for 520 m, and, up to 2007, 475 m were replaced (Fig. 15). The NEG coating was done by SAES Getter [69–71] in Milan, Italy. Figure 16 shows a typical NEG section bakeout and activation cycle.

The effect of the NEG coated beam pipes can be seen in Figs. 15 and 17. Figure 17 shows that the dynamic pressure in the 12 Blue warm sections in 2004, 2005, and 2006 decreases by orders of magnitude even with increasing
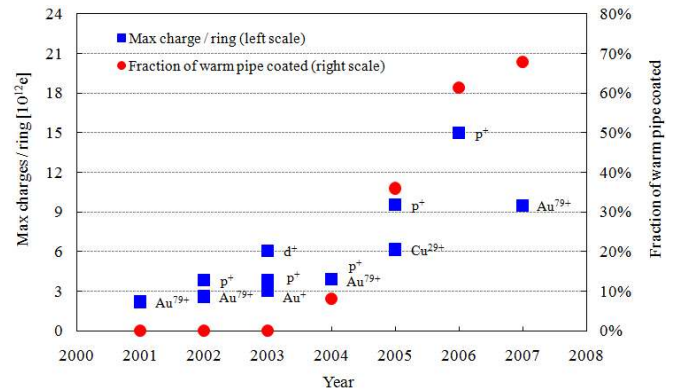

FIG. 15. (Color) Total charge of RHIC beams versus fraction of warm beam pipes coated with NEG. Large-scale application of NEG pipes began in 2005. Note that the intensity of gold beams is also constrained by the injectors and intrabeam scattering, and the intensity of polarized protons by the beam-beam interaction.

beam intensity. Figure 15 shows that the total number of charges per ring increases in 2006 and 2007 together with the length of the installed NEG coated beam pipes. Note that the Au intensity in 2007 is limited by the injectors, intrabeam scattering, and instabilities at transition, and the intensity of polarized protons by the beam-beam interaction.

C. Solenoids

In 2003, 60 m of solenoids were installed in the warm sections to evaluate their effect on the dynamic pressure. Solenoids had been successfully used in other machines to suppress electron clouds, for example, in KEKB [72], PEP-II [5], and BEPC [73].

Since the electron motion mainly develops in the transverse direction, longitudinal solenoid fields force electrons to follow circlelike orbits. Hence, electrons created at the chamber's surface are kept close to the chamber wall, the electron energy gain is small and the SEY of the electron-wall collision is reduced. All this results in an effective mitigation of the multipacting effect.
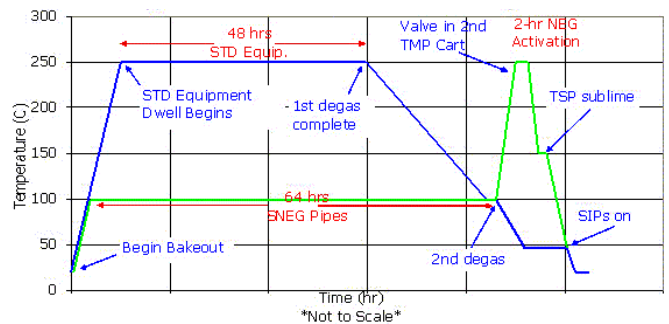

FIG. 16. (Color) Typical NEG section bakeout and activation. After all surrounding components have been baked at 250°C, the NEG surface is activated.

W. FISCHER *et al.*

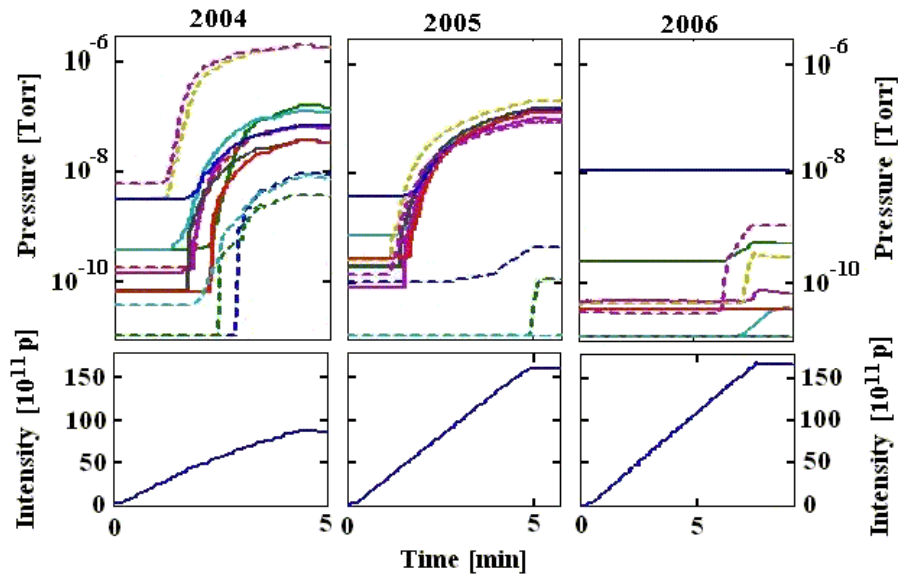Phys. Rev. ST Accel. Beams **11,** 041002 (2008)

FIG. 17. (Color) Dynamic pressure in the 12 Blue warm straight sections (top), measured by a single gauge in each, while proton beam with 108 ns bunch spacing is filled (bottom). Data was obtained in 2004–2006. The beam conditions were chosen for comparison of dynamic pressure rise, not for typical operations. With completely NEG coated pipes, the pressure in 3 sections in 2005, and 5 sections in 2006, remained at 10^{-11} Torr [63].

The strength of the solenoidal field should be such that the Larmor radius of the electron trajectory must be much smaller than the beam pipe radius r. Otherwise the trajectory is not sufficiently bent and the electron trajectory not too different from the case without a solenoidal field. For an electron with energy E, this is expressed by

$$\frac{\sqrt{2m_e E}}{eB} \ll r, \tag{18}$$

where m_e is the electron mass and B the solenoidal field. Experimental evidence of the multipacting mitigation at RHIC is shown in Fig. 18. It shows the vacuum pressure in
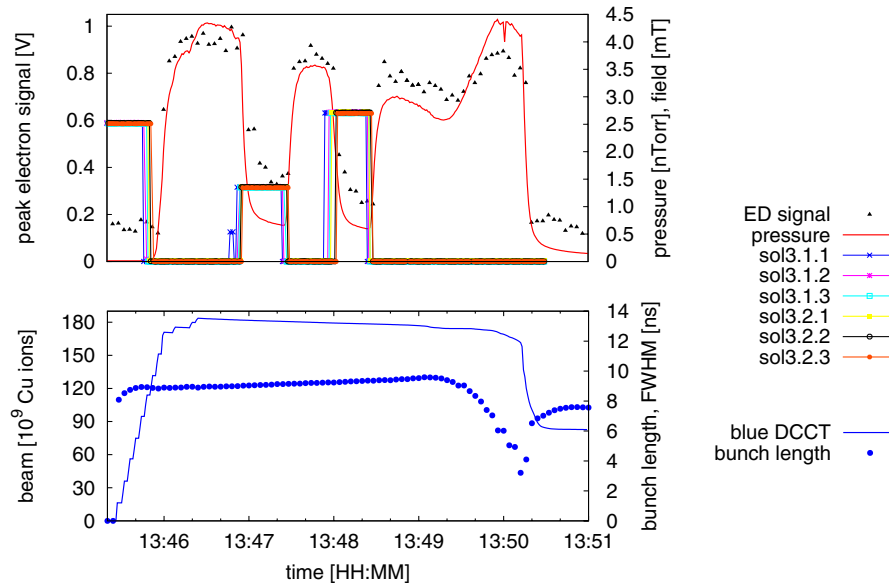

FIG. 18. (Color) Effect of the solenoid field at BI12, where 90% of the entire section is covered with solenoids. A solenoidal field of 1.35 mT is enough to decrease the pressure by about a factor 7. No further improvements are noticeable when the field is increased to 2.7 mT (see text). At about 13:49:30, the acceleration ramp starts, the bunch length is reduced, and pressure and electron signals increase. Half of the beam is lost while crossing the transition energy (13:50:05), after which the electron cloud disappears because of the low bunch intensity [43].

the straight section called "BI12," where almost 90% of the beam pipe is covered by solenoids. It can be seen that a solenoidal field of 1.35 mT decreases the pressure by about a factor of 7 (from 43 to 6 nTorr), and that the pressure is not reduced much further when the field is increased to 2.7 mT. This is consistent with Eq. (18). For $B = 1.35$ mT, the Larmor radius of an electron with an energy of 5 eV is 5.5 mm (the RHIC beam pipe radius is $r = 6$ cm), sufficient to suppress multipacting. Recall the large contribution of low energy electrons around 5 eV to the energy spectrum at RHIC (Fig. 11).

Given the decay times for the pressure, the observation is consistent with the expected pressure reduction. Even if the solenoids fully suppress the cloud, there is still a fraction of the beam pipe at BI12 (around 10%) where one has a gas load due to electron-impact desorption. Thus, the pressure can only be decreased by about a factor of 10. The region not wrapped by the solenoids at BI12 is the tee and surrounding area where the vacuum pump and electron detector are located. This implies that at the electron detector location the multipacting electrons are not affected by a uniform solenoid field. In fact, the electron signal shown in Fig. 18 decreases while the solenoid fields increase, yet a complete suppression does not occur even at 2.7 mT. A quantitative analysis of the electron signal behavior under these circumstances is cumbersome.

Different electron cloud computer simulation codes have been used to study the electron cloud at RHIC in the presence of a uniform and constant solenoid field. Reference [43] reproduces the case shown in Fig. 18 and shows that a 1 mT field fully suppresses the electron cloud formation.

A number of reasons led to the decision to favor NEG coated beam pipes over solenoids for large-scale installation in the warm areas. At comparable cost per unit length, NEG was more effective in reducing beam induced pressure increases. While both solenoids and NEG surfaces reduce electron clouds, only the NEG surfaces also reduce the pressure caused by other sources. With continuous operation, solenoids also increase the beam pipe temperatures and lead to higher thermal outgassing. Finally, after activation, operation and maintenance of NEG coated beam pipes is simpler and more reliable than the operation of solenoids with many small power supplies. Solenoids are still used near some experimental areas, and near some equipment that cannot be baked at high temperature.

D. Bunch patterns

When machines are operated with less than the maximum number of bunches, the flexibility of rearranging the intensity in different bunch patterns can be used to minimize the electron cloud density and to maximize the luminosity in a collider. With round beams, as usually found in ion colliders, the luminosity can be written as

$$\mathcal{L} = F(\beta\gamma)\frac{f_0}{4\pi}N_a\frac{N_{b1}N_{b2}}{\beta^*\epsilon_N}, \qquad (19)$$

where $(\beta\gamma)$ is the relativistic factor, f_0 is the revolution frequency, N_a is the number of bunches, N_{b1} and N_{b2} are the number of ions per bunch in the two beams, respectively, β^* is the lattice function at the collision point (assumed to be the same for the horizontal and vertical plane and for both rings), ϵ_N the normalized rms emittance (also the same for all transverse planes in both rings), and F a factor that accounts for the hourglass effect and a possible crossing angle. The same total intensity gives a higher luminosity when concentrated in fewer bunches.

To minimize the peak and average electron cloud density, simulations and experiments show that it is best to, first, distribute any given number of bunches approximately uniformly around the ring [74], and second, con-
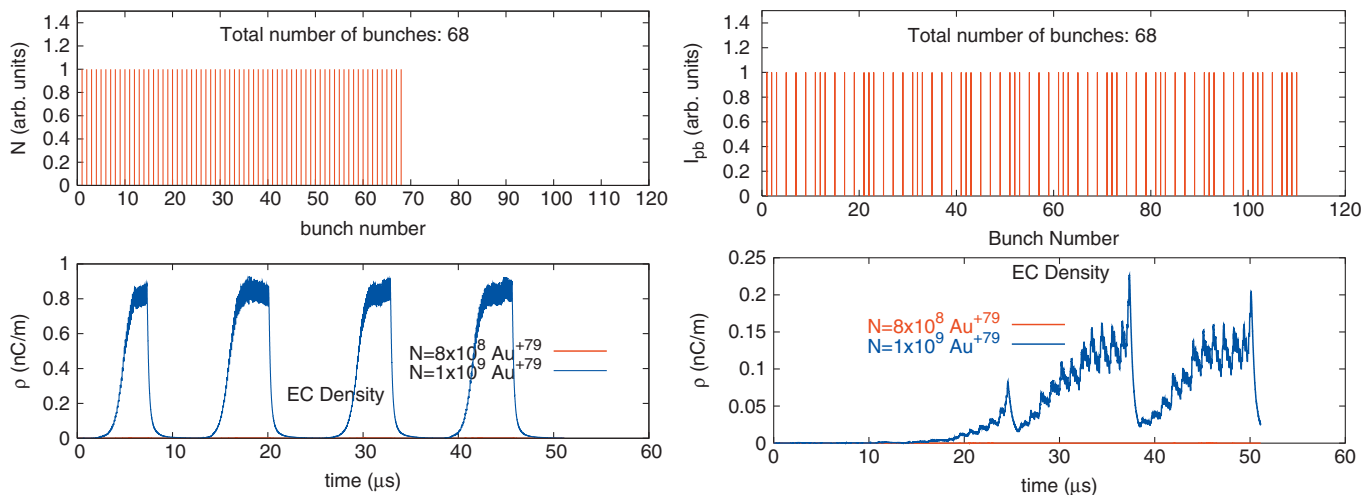

FIG. 19. (Color) Simulated electron cloud evolution over 4 turns for 68 Au bunches with a single gap of maximum lengths (top), and 68 bunches distributed approximately uniformly around the circumference [74].

centrate any given intensity in as few bunches as possible. The latter condition also maximized the luminosity.

The effect of different distributions around the ring, with a fixed number of bunches, is shown in Fig. 19. The top plot shows the simulated electron cloud density over 4 turns for 68 Au bunches with a single gap of maximum length, the bottom shows the simulated electron cloud density for 68 Au bunches distributed approximately uniformly around the circumference. For the latter case, the peak electron cloud density is reduced by about a factor 5, the average electron cloud density even more. The problem of optimizing bunch pattern lends itself to analysis through maps for electron clouds [75].

In Fig. 20 the peak and average electron cloud densities are shown for different numbers of bunches and the same total intensity. The average electron cloud density increases from bunch numbers 36 to 68, and then is approximately constant up to 111 bunches. The maximum electron cloud density reaches a maximum for 78 bunches and generally trends downwards for both greater and fewer bunches, although the trends are not entirely monotonic. The jitter in the peak intensity is likely due to the fact that bunches can only be placed in rf buckets, and the resulting gaps are not exactly uniformly distributed. To minimize the electron-impact desorption, it is best to minimize the average electron cloud density; to minimize instabilities in all bunches, it is best to minimize the maximum electron cloud density.

Based on these simulations, the bunch patterns were optimized during the RHIC runs in 2004 and 2005. In the 2004 run (Au-Au), the beam intensity and luminosity was limited by dynamic pressure rises in the PHOBOS experiment (Fig. 4), that led to unacceptable experimental background [33]. During the run the number of bunches was reduced from 61 to 56 to 45, all approximately uniformly distributed, as more bunch intensity became available from the injectors. This allowed an increase in the luminosity while operating at the electron cloud limit in PHOBOS.

FIG. 21. (Color) Single slice of a 0.2 mm × 50 mm surface scan of RHIC beam pipe material obtained by Solarius, Inc. [83] using an optical profilometer. An ion trajectory incident at 1 mrad is superimposed, showing multiple transitions between vacuum and solid [25].

The same limit remained in place for the 2005 Cu-Cu run. With Cu the injectors could deliver even more charges per bunch, and the number of bunches could be further reduced to 37.

E. Antigrazing rings

Lost beam particles hitting the beam pipe under a grazing incident angle penetrate the beam pipe surface many times due to the surface roughness (Fig. 21). This is expected to lead to electron and molecular desorption coefficients about 2 orders of magnitude higher than for perpendicular impact. In Ref. [25] a mitigation technique was proposed which consisted of installing antigrazing rings, through which all particles are lost with near perpendicular impact. For a test 5 antigrazing rings (Fig. 22) were installed in each of 2 sections in RHIC, and a reduction in the dynamic pressure rise could be observed (Fig. 23) [76].
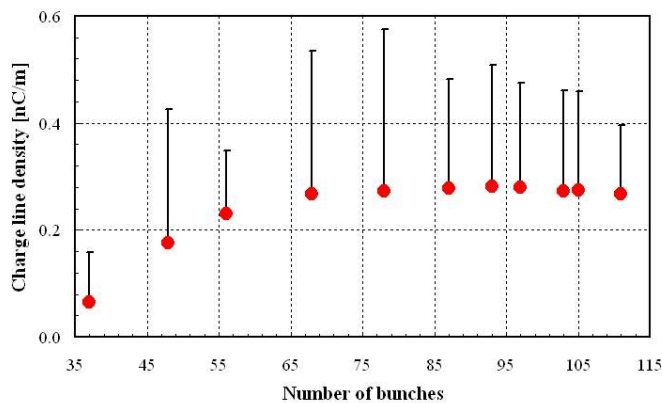

FIG. 20. (Color) Simulated average (red dots) and peak (bars) electron cloud density as a function of the number of bunches where the total intensity is held constant.
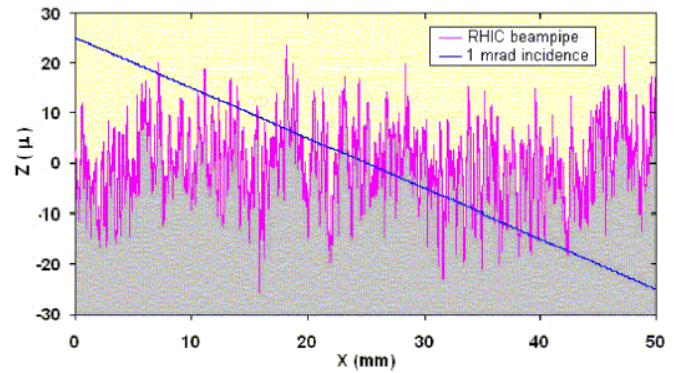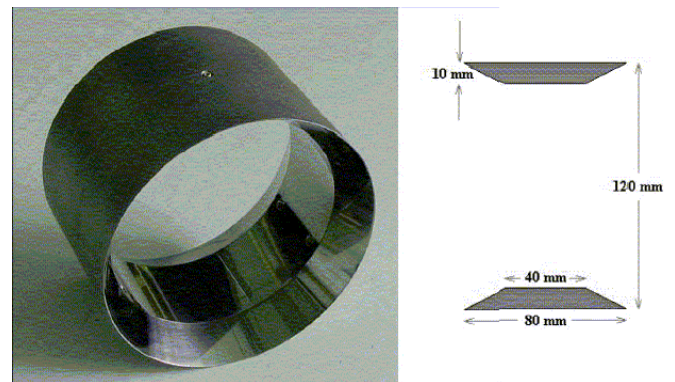

FIG. 22. (Color) Photograph and cross-sectional view of one of the antigrazing rings. In the photograph one of 5 set screws is visible. The tapering of the rings edges is introduced to further reduce their already small impact on the ring impedance [25].
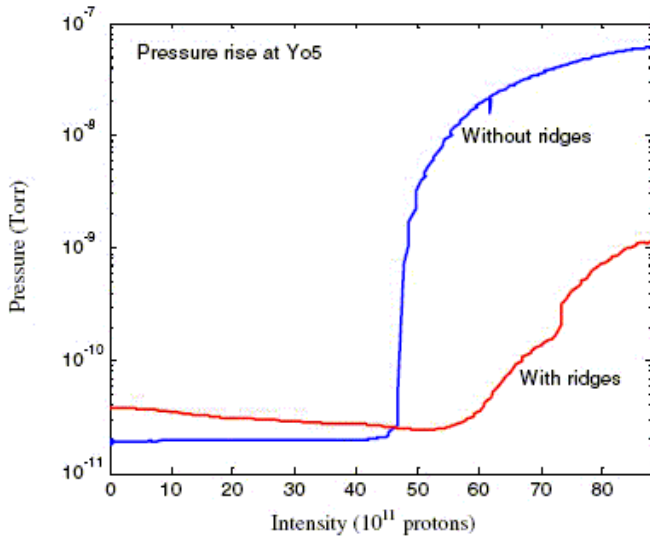
FIG. 23. (Color) Dynamic pressure in warm section YO5 when 111 proton bunches with approximately 1.5×10^{11} protons/bunch are injected, without and with antigrazing rings [76].

However, for the grazing rings to be effective, they must intercept beam, which could lead to increased experimental background if they are close to a detector and the beam intercepted there would be otherwise lost elsewhere. With the large-scale installation of NEG coated beam pipes, it was decided not to employ antigrazing rings in RHIC for now.

F. Prepumping in cold sections

At high proton beam intensities an increase in the gas density in the cold sections was observed (Fig. 24). The cold sections initially relied on cryopumping, and had been evacuated before cooldown with mobile turbo pumps to about 10^{-1} Torr only in some areas. The surface density σ of gas molecules after cooldown is

$$\sigma = \frac{Pr}{2kT}, \tag{20}$$

where P and T are the pressure and temperature before cooldown, respectively, r the beam pipe radius, and k the Boltzmann constant. For a flat surface, a monolayer has of order 10^{19} molecules/m^2 [77], and a pressure of 10^{-1} Torr before cooldown will result in about 5 monolayers. Near a warm-cold transition there can be many more monolayers.

After the observation of an increased gas density in the cold arcs, small ion pumps were installed permanently in these regions, which evacuated the beam pipe to 10^{-6} to 10^{-7} Torr before cooldown of the magnets, leading to much less than a monolayer of gas on the cold beam pipe surface. With the added pumps no further increases in the gas density were observed.
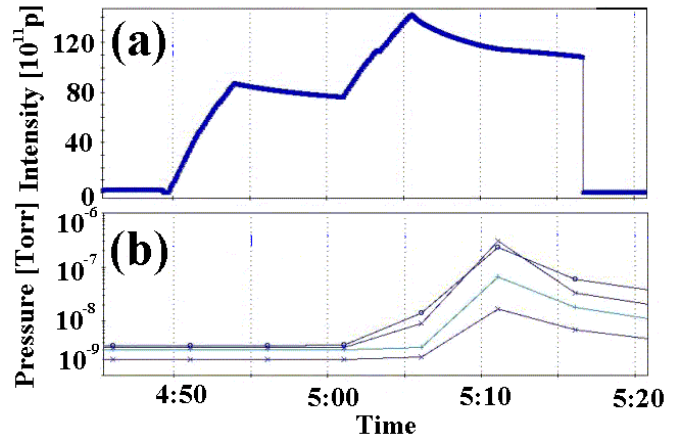

FIG. 24. (Color) Increase of gas density in cold arcs (b), as measured by 4 gauges, when protons are injected (a). The increase of the gas density is measured with a warm gauge connected to the cold vacuum through a small diameter conduit.

G. Beam scrubbing

Scrubbing with beam is used routinely in the SPS [4,78]. In RHIC scrubbing had been tested first in 2004 [79]. With scrubbing times of a few hours a reduction of the dynamic pressure rise by some 10% was observed in locations with the highest pressure. Scrubbing was most efficient in locations with large dynamic pressures.

At the beginning of the 2007, gold-gold run pressures up to 10^{-6} Torr were observed near the warm rf and a few other locations that cannot be baked at high temperature. Two hours of scrubbing at injection with the highest available ion intensities, and seven fills, reduced the dynamic
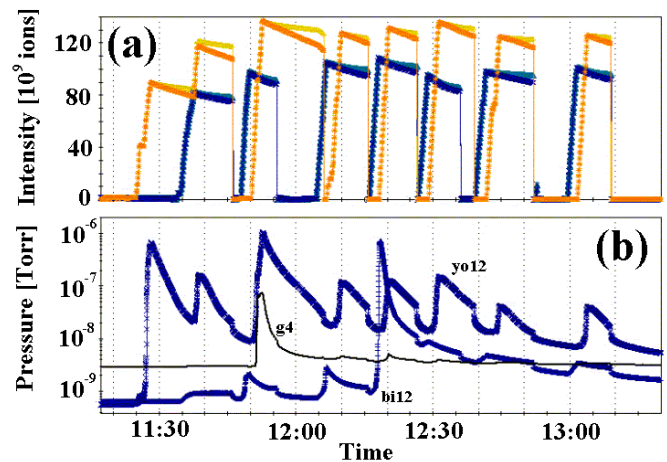

FIG. 25. (Color) Beam scrubbing during the 2007 Au operation. Part (a) shows the Blue and Yellow intensities over 2 hours when the machine was repeatedly filled with the highest available intensities. Part (b) shows the pressure near the warm rf (labeled g4) and the Blue and Yellow polarimeters (labeled bi12 and yo12, respectively), the 3 locations with the highest pressure. The dynamic pressure at these locations is reduced by more than an order of magnitude after scrubbing.

pressure by approximately 1 order of magnitude at the locations with the highest pressure (Fig. 25). Scrubbing can also be seen in the reduction of the electron-impact desorption coefficient η_e of unbaked stainless steel over the length of a run (Fig. 12 top).

H. Operation with longer bunches

The electron cloud in RHIC is enhanced with shortened bunches. This is observable at injection, transition, and store when the bunches are shortened by a factor 2 before they are transferred into the storage rf system (see Fig. 5).

At transition, the rf voltage has been reduced from 300 to 150 kV to lengthen the bunches, and reduce the electron cloud density. In experiments it was observed that the intensity loss along the bunch train can be reduced in this way [50].

A small longitudinal emittance of proton beams is desirable to reduce the hourglass effect in collision [80]. In 2006, proton stores started with an hourglass factor of typically 0.75. Protons are injected close to and above the transition energy, where longitudinal matching is only possible when the bunches are shortened through quadrupole pumping in the AGS before transfer to RHIC. This, however, enhances the electron cloud, and may have led to incoherent emittance growth. To allow for the injection of matched bunches without an enhancement of the electron cloud density, a new rf system with harmonic number 120 is under construction (the existing acceleration system has harmonic number 360) [81]. The new cavity is common to both rings and will also ensure that the rf frequencies of the two rings are locked at all times to avoid parameter modulations from the beam-beam interaction on the ramp [82].

IV. SUMMARY

Since 2001, electron cloud effects have limited the beam intensity in RHIC. The most common effect is dynamic pressure rise. This occurred with all species at injection, transition (except protons that do not cross the transition energy), and store. In some cases, pressure instabilities were observed. Various pressure rise mechanisms were investigated and it was concluded that all operationally relevant dynamic pressure increases are caused by electron clouds.

The beam intensity can also be limited because electron clouds lower the instability threshold of bunches crossing the transition energy. Recently, incoherent transverse emittance growth has been observed with protons at injection, possibly caused by electron clouds.

The main cure for electron clouds in the warm sections of RHIC is NEG coated beam pipes, which have a lower secondary electron yield than bare stainless steel pipes, and provide additional pumping. By now almost all beam pipes that can be NEG coated have been replaced. In the cold regions, additional pumps reduced the pressure in the beam pipe before cooldown, leading to much less than a mono-layer of molecules on the wall when the pipe is cold. Other cures tested, or used in limited regions, include solenoids, optimized bunch patterns, antigrazing rings, and scrubbing.

RHIC is operating close to the dynamic pressure limit in selected warm areas that cannot be baked at high temperatures and, except for the case of proton beams, is close to the instability threshold at transition. The possible incoherent emittance growth of proton beams at injection is expected to be mitigated by a new rf system, which allows injection of longer bunches while maintaining the longitudinal emittance. If electron clouds still remain an operational problem, scrubbing will be needed to improve the machine performance.

[1] W. Fischer, *Proceedings of the 2006 European Particle Accelerator Conference, Edinburgh, UK* (EPS-AG and CERN, Geneva, 2006), pp. 905–909.

[2] W. Fischer, "Run overview of the Relativistic Heavy Ion Collider," http://www.rhichome.bnl.gov/RHIC/Runs/ (2007).

[3] A. Drees, Report No. BNL RHIC/AP/150, 1998.

[4] G. Arduini *et al.*, Proceedings ECLOUD'04, 31st Advanced ICFA Beam Dynamics Workshop on Electron-Cloud Effects, Napa, CA, Report No. CERN-2005-001, CARE-Conf-05-001-HHH, LBNL-56372, SNS-104000000-TR0024-R00, pp. 31–47 (2005).

[5] A. Kulikov, A. Novokhatski, and J. Seeman, Proceedings ECLOUD'04, Napa, CA, Ref. [4], pp. 21–24.

[6] R. J. Macek *et al.*, Proceedings ECLOUD'04, Napa, CA, Ref. [4], pp. 63–75.

[7] R. Zwaska, *Proceedings ECLOUD'07, International Workshop on Electron-Cloud Effects, Daegu, Korea*, KEK Proceedings 2007-10 (KEK, Tsukuba, 2007), p. 37.

[8] O. Gröbner and R. S. Calder, *Proceedings 1973 Particle Accelerator Conference, San Francisco, CA*, IEEE Transactions on Nuclear Science (IEEE, Piscataway, NJ, 1973), Vol. NS-20, No. 3, pp. 760–764.

[9] S. Y. Zhang and L. A. Ahrens, *Proceedings of the 1999 Particle Accelerator Conference, New York* (IEEE, Piscataway, NJ, 1999), pp. 3294–3296.

[10] A. Smolyakov, W. Fischer, C. Omet, and P. Spiller, Report No. GSI-Acc-Report-2005-11-001, 2005; Report No. BNL C-A/AP/117, 2006.

[11] P. J. Spiller, K. Blasche, P. Hülsmann, A. Krämer, H. Ramakers, H. Reich-Sprenger, *Proceedings of the 2004 European Particle Accelerator Conference, Lucerne, Switzerland* (EPS-AG and CERN, Geneva, 2004), pp. 1180–1182.

[12] H. Kollmus, M. C. Bellachioma, M. Bender, A. Krämer, J. Kurdal, and H. Reich-Sprenger, Proceedings of the 2006 European Particle Accelerator Conference, Edinburgh, UK, Ref. [1], pp. 1426–1428.

[13] J. Pasternak, C. Bal, C. Carli, M. Chanel, and E. Mahner, *Proceedings of the 2005 Particle Accelerator Conference, Knoxville, TN* (IEEE, Piscataway, NJ, 2005), pp. 3816–3818.

[14] W. Fischer *et al.*, *Proceedings of the 2002 European Particle Accelerator Conference, Paris, France* (EPS-GA and CERN, Geneva, 2002), pp. 1485–1486.

[15] U. Iriso *et al.*, Proceedings of the 2004 European Particle Accelerator Conference, Lucerne, Switzerland, Ref. [11], pp. 2239–2241.

[16] S. Y. Zhang *et al.*, Proceedings of the 2006 European Particle Accelerator Conference, Edinburgh, UK, Ref. [13], pp. 4308–4310.

[17] Y.-K. Kim *et al.*, http://physics.nist.gov/PhysRefData/Ionization/ (2004).

[18] O. Gröbner, CERN Report No. 99-05, 1999, p 132.

[19] F. F. Rieke and W. Prepejchal, Phys. Rev. A **6**, 1507 (1972).

[20] W. Fischer, J. M. Brennan, M. Blaskiewicz, and T. Satogata, Phys. Rev. ST Accel. Beams **5**, 124401 (2002).

[21] U. Iriso and W. Fischer, Phys. Rev. ST Accel. Beams **8**, 113201 (2005).

[22] U. Iriso and W. Fischer, Phys. Rev. ST Accel. Beams **9**, 029901 (2006).

[23] U. Iriso, P. He, H. C. Hseuh, H. Huang, V. Ptitsyn, L. Smart, P. Thieberger, D. Trbojevic, and S. Y. Zhang, Report No. BNL C-A/AP/178, 2004.

[24] H. Huang *et al.*, Proceedings of the 2006 European Particle Accelerator Conference, Edinburgh, UK, Ref. [1], pp. 583–585.

[25] P. Thieberger, W. Fischer, H. C. Hseuh, V. Ptitsyn, L. P. Snydstrup, D. Trbojevic, and S. Y. Zhang, Phys. Rev. ST Accel. Beams **7**, 093201 (2004).

[26] W. Fischer, H. C. Hseuh, U. Iriso, and E. Mustafin, Proceedings ECLOUD'07, International Workshop on Electron-Cloud Effects, Daegu, Korea, Ref. [7], pp. 76—80.

[27] G. Rumolo and F. Zimmermann, Report No. CERN-SL-2001-014 AP, 2001.

[28] M. Inokuti, Rev. Mod. Phys. **43**, 297 (1971).

[29] W. C. Turner (unpublished).

[30] W. Fischer and U. Iriso, Report No. BNL C-A/AP/184, 2004.

[31] S. Y. Zhang, Report No. BNL C-A/AP/198, 2005.

[32] U. Iriso and S. Peggs, Phys. Rev. ST Accel. Beams **9**, 071002 (2006).

[33] G. Rumolo and W. Fischer, Report No. BNL C-A/AP/146, 2004.

[34] S. Y. Zhang, Report No. BNL C-A/AP/190, 2005.

[35] W. Fischer, U. Iriso, and E. Mustafin, *Proceedings 33rd ICFA Beam Dynamics Workshop on High Intensity and High Brightness Beams, Bensheim, Germany*, AIP Conf. Proc. No. 773 (AIP, New York, 2004), pp. 204–206.

[36] E. Mustafin, I. Hofmann, P. Spiller, W. Fischer, U. Iriso, P. He, H. C. Hseuh, V. Ptitsyn, and S. Y. Zhang, *Proceedings 33rd ICFA Beam Dynamics Workshop on High Intensity and High Brightness Beams, Bensheim, Germany* (Ref. [35]), pp. 222–225.

[37] M. A. Furman and A. A. Zholents, *Proceedings of the 1999 Particle Accelerator Conference, New York*, Ref. [9], pp. 1794–1796.

[38] F. Zimmermann, *Proceedings of the 1999 Particle Accelerator Conference, New York*, Ref. [9], pp. 666–670.

[39] K. Ohmi, S. Heifets, and F. Zimmermann, *Proceedings of the Asian Particle Accelerator Conference, Beijing, 2001* (Institute of High Energy Physics, Beijing, 2001), pp. 445–447; Report No. CERN SL-2001-062 (AP), 2001.

[40] M. Blaskiewicz and U. Iriso, Report No. BNL C-A/AP/260, 2006.

[41] M. Blaskiewicz, M. A. Furman, M. Pivi, R. J. Macek, Phys. Rev. ST Accel. Beams **6**, 014203 (2003).

[42] M. A. Furman and M. Pivi, Phys. Rev. ST Accel. Beams **5**, 124404 (2002).

[43] U. Iriso, Ph.D. thesis, University of Barcelona (Report No. BNL C-A/AP/228, 2006).

[44] U. Iriso *et al.*, *Proceedings for the 2003 Particle Accelerator Conference, Portland, OR* (IEEE, Piscataway, 2003), pp. 794–796.

[45] R. Macek *et al.*, Proceedings of the International Workshop on Two-Stream Instabilities in Particle Accelerator and Storage Rings, Tsukuba, Japan, 2001, http://conference.kek.jp/two-stream/.

[46] R. A. Rosenberg and K. C. Harkay, Nucl. Instrum. Methods Phys. Res., Sect. A **453**, 507 (2000).

[47] U. Iriso and J.-M. Laurent, LHC-VAC CERN, Technical report TN03-05, 2003.

[48] Z. Y. Guo, *Proceedings of the 2001 Particle Accelerator Conference, Chicago, IL* (IEEE, Piscataway, NJ, 2001), pp. 676–678.

[49] M. Blaskiewicz *et al.*, Proceedings for the 2003 Particle Accelerator Conference, Portland, OR, Ref. [44], pp. 3026–3028.

[50] J. Wei *et al.*, Proceedings of the 39th ICFA Advanced Beam Dynamics Workshop on High Intensity High Brightness Hadron Beams HB2006, Tsukuba, Japan (2006).

[51] V. Ptitsyn (private communication).

[52] F. Zimmermann, Phys. Rev. ST Accel. Beams **7**, 124801 (2004).

[53] G. Rumolo, A. Z. Ghalam, T. Katsouleas, C. K. Huang, V. K. Decyk, C. Ren, W. B. Mori, F. Zimmermann, and F. Ruggiero, Phys. Rev. ST Accel. Beams **6**, 081002 (2003).

[54] E. Benedetto, D. Schulte, F. Zimmermann, and G. Rumolo, Phys. Rev. ST Accel. Beams **8**, 124402 (2005).

[55] E. Benedetto, G. Franchetti, and F. Zimmermann, Phys. Rev. Lett. **97**, 034801 (2006).

[56] K. Ohmi and K. Oide, Phys. Rev. ST Accel. Beams **10**, 014401 (2007).

[57] S. Y. Zhang and V. Ptitsyn, Report No. BNL C-A/AP/257,

2006.

[58] S. Y. Zhang and V. Ptitsyn, Proceedings ECLOUD'07, International Workshop on Electron-Cloud Effects, Daegu, Korea, Ref. [7], pp. 172–177.

[59] C. Benvenuti *et al.*, Vacuum **60**, 57 (2001).

[60] C. Benvenuti *et al.*, J. Vac. Sci. Technol. A **16**, 148 (1998).

[61] M. Hahn, R. Kersevan, and I. Parat, Proceedings of the 2006 European Particle Accelerator Conference, Edinburgh, UK, Ref. [1], pp. 1420–1422.

[62] S. Y. Zhang, H. C. Hseuh, W. Fischer, H. Huang, and T. Roser, Report No. BNL C-A/AP/220 (2005).

[63] S. Y. Zhang *et al.*, Proceedings of the 2006 European Particle Accelerator Conference, Edinburgh, UK, Ref. [1], pp. 595–597.

[64] A. Nadji, *Proceedings of the 2007 Particle Accelerator Conference, Albuquerque, NM* (IEEE, Piscataway, NJ, 2007), pp. 932–934.

[65] P. Chiggiato and P. Costa Pinto, Thin Film Solids **515**, 382 (2006).

[66] A. Rossi, Proceedings ECLOUD'04, 31st Advanced ICFA Beam Dynamics Workshop on Electron-Cloud Effects, Napa, CA, Ref. [4], pp. 113–117.

[67] C. Scheuerlein, B. Henrist, N. Hilleret, and M. Taborelli, Appl. Surf. Sci. **172**, 95 (2001).

[68] M. Nishiwaki and S. Kato, Proceedings ECLOUD'07, International Workshop on Electron-Cloud Effects, Daegu, Korea, Ref. [7], pp. 82–85.

[69] Company web site www.saesgetters.com.

[70] A. Bonucci, A. Conte, P. Manini, and S. Raimondi, Proceedings of the 2007 Particle Accelerator Conference, Albuquerque, NM, Ref. [64].

[71] A. Conte, P. Manini, S. Raimondi, and A. Bonucci, Proceedings of the 2007 Particle Accelerator Conference, Albuquerque, NM, Ref. [64], pp. 212–214.

[72] H. Fukuma, Proceedings ECLOUD'04, 31st Advanced ICFA Beam Dynamics Workshop on Electron-Cloud Effects, Napa, CA, Ref. [4], pp. 15–19.

[73] J. Q. Wang, Z. Y. Guo, Y. D. Liu, Q. Qin, J. Xing, and Z. Zhao, Phys. Rev. ST Accel. Beams **7**, 094401 (2004).

[74] W. Fischer and U. Iriso, Proceedings of the 2004 European Particle Accelerator Conference, Lucerne, Switzerland, Ref. [11], pp. 914–916.

[75] U. Iriso and S. Peggs, Phys. Rev. ST Accel. Beams **8**, 024403 (2005).

[76] S. Y. Zhang, H. C. Hseuh, P. Thieberger, and D. Trbojevic, Phys. Rev. ST Accel. Beams **8**, 123201 (2005).

[77] M. Bender, Diploma thesis, Fachhochschule Wiesbaden, GSI Diploma 2003-11, 2003.

[78] J.-M. Jiménez *et al.*, Proceedings for the 2003 Particle Accelerator Conference, Portland, OR, Ref. [44], pp. 307–311.

[79] S. Y. Zhang *et al.*, Proceedings of the 2004 European Particle Accelerator Conference, Lucerne, Switzerland, Ref. [11], pp. 947–949.

[80] M. A. Furman and M. S. Zisman, in *Handbook of Accelerator Physics and Engineering*, edited by A. W. Chao and M. Tigner (World Scientific, Singapore, 2006), pp. 277–281.

[81] M. Brennan and A. Zaltsman (private communication).

[82] W. Fischer, P. Cameron, S. Peggs, and T. Satogata, Report No. BNL C-A/AP/72, 2002.

[83] Solarius Development Inc., Sunnyvale, CA, USA.